

An electrochemically stable defect-free glassy electrolyte formed at room temperature for all-solid-state sodium batteries

Xiaowei Chi

2Shanghai Institute of Ceramics, Chinese Academy of Sciences

Ye Zhang

University of Houston

Fang Hao

University of Houston

Steven Kmiec

Iowa State University

Hui Dong

University of Houston

Rong Xu

Purdue University

Kejie Zhao

Purdue University

Liang Wang

Northern Illinois University

Lihong Zhao

University of Houston

Liqun Guo

University of Houston

Huolin Xin

University of California, Irvine

Steve Martin

Iowa State University

Yan Yao (✉ yyao4@Central.UH.EDU)

University of Houston <https://orcid.org/0000-0002-8785-5030>

Article

Keywords: batteries, all-solid-state sodium batteries (ASSSBs), solid electrolyte (SE), room-temperature processing, glassy network structure

Posted Date: September 28th, 2021

DOI: <https://doi.org/10.21203/rs.3.rs-934971/v1>

License:  This work is licensed under a Creative Commons Attribution 4.0 International License.

[Read Full License](#)

Abstract

All-solid-state sodium batteries (ASSSBs) are promising candidates for grid-scale energy storage applications. To date, however, there are no commercialized ASSSBs due in part to the lack of a solid electrolyte (SE) that meets all of the requirements of low cost, facile fabrication, high Na^+ conductivity, electrochemical stability, and is resistant to sodium metal dendrite penetration. In this work, we report a family of oxysulfide glass SEs ($\text{Na}_3\text{PS}_{4-x}\text{O}_x$, where $0 < x \leq 0.6$) that combine the advantages of sulfides and oxides, we demonstrate stable electrochemical cycling of Na metal for hundreds of hours and the highest critical current density of 2.3 mA cm^{-2} among all Na-ion conducting sulfide-based SEs. These performance enhancements are found to be associated with the ability of the oxysulfide glass to undergo room temperature pressure induced amorphization that creates a fully homogeneous glass structure that has robust mechanics and substantial chemical and electrochemical stability. Microstructural analysis revealed that the added oxygen creates a glassy network structure by forming bridging oxygen units resulting in a significantly stronger defect-free glass network and two orders of magnitude lower electronic conductivity compared to the fully ionic and non-network structure of Na_3PS_4 . We show ambient-temperature sodium-sulfur batteries (ATSSBs) can be fabricated from these SEs that demonstrate the highest specific energy among the current sodium batteries. The unique room-temperature processing of composite SE structures may provide a sustainable path forward for the further development of ATSSBs in particular and ASSSBs in general.

Full Text

Low-cost batteries with high safety and specific energy are in ever-increasing demand for grid-scale energy storage¹. All-solid-state sodium batteries (ASSSBs) using nonflammable solid-state electrolytes (SEs) and earth-abundant sodium metal anodes are among the most promising and therefore are attracting worldwide research attention²⁻⁵. So far, the only successful example of a commercialized Na metal anode battery for grid-scale energy storage is the well-known high-temperature sodium-sulfur battery⁶. However, at the high working temperature of $>300 \text{ }^\circ\text{C}$, both Na anode and S cathode are liquids, dramatically increasing the operational cost and decreasing the safety due to fires and explosions caused by the catastrophic failure of the thin ceramic SE⁷. In contrast, ambient-temperature ASSSBs using solid Na metal anodes are significantly more desirable not only because they are lower cost, but their lower temperature operation, $T \ll 100 \text{ }^\circ\text{C}$, enables them to be more safely used in a broader range of applications. However, when operated such that the Na metal anode is now in the solid state, not only must the SE be resistant to direct chemical and electrochemical reaction with Na, it must also be resistant to solid metallic sodium dendrite penetration. Therefore, the search of new SEs for ASSSBs must simultaneously meet the stringent requirements of low cost and facile fabrication, but also meet severe mechanical and chemical stability requirements. So far, no single sodium SE has been able to simultaneously meet all four of these requirements and therefore, the development of SEs that are stable while cycling solid Na metal remains of great challenges.

Inorganic SEs can be divided into three categories, ceramic, glass-ceramic, and glass. Ceramic SEs such as $\beta''\text{-Al}_2\text{O}_3$ and NASICON-type oxides exhibit excellent chemical stability towards Na metal, nevertheless, their high Na^+ conductivities are achieved only when they are processed to near theoretical densities requiring sintering temperatures in excess of 1,500 °C for long hours, are subjected to poor wettability with Na metal due to their rigid and rough surface^{8,9}. Additionally, Na metal has been observed to preferentially propagate along distinct grain boundaries forming dendrites which eventually short circuit the electrolyte^{10,11} (**Scheme 1a**). This has been a source of controversy in the field of SEs because these ceramic oxide SEs have mechanical moduli in excess of 200 GPa and provide more than adequate elastic and shear moduli to resist Na dendrite. Glass-ceramic SEs (e.g., Na_3PS_4) and other sulfide SEs have compliantly soft surfaces which exhibit less well-defined grain boundaries due to the existence of a certain quantity of a glassy phase (5~50 vol%), which can mitigate the dendrite formation and growth. However, when contacting with Na metal, these SEs are unstable at reducing potential (0V vs Na/Na^+), and therefore decompose to an unstable solid electrolyte interphase (SEI) layer¹²⁻¹⁵ (**Scheme 1b**). For these reasons, Na alloys such as Na-Sn are commonly applied as an alternative anode, but these raise the voltage on the anode and severely decrease the specific energy density.

To date, there is no single SE that can simultaneously meet all of the mechanical, chemical, electrochemical, and processing requirements that can enable the ASSSB with enhanced electrochemical performance and specific energy. While Lazar et al. have reported the chemical stability of the mixed oxy-sulfide $\text{Na}_3\text{PS}_3\text{O}_1$ SE in contact with metallic Na when pressed into an amorphous phase¹⁶, they have not conducted any electrochemical or cell level work on these amorphous phases. Here, knowing the specific benefits of the individual SEs described above, and recognizing the inherent cost, process, and scale-up advantages of the mechano-chemical milling (MCM), we report in this work a series of $\text{Na}_3\text{PS}_{4-x}\text{S}_x$ oxysulfide glass SEs that consist of a predominantly sulfide-based SE that is doped with small amounts, up to 15 mol.%, of oxygen, that can be rendered fully chemically reacted from simple precursors by MCM and fully glassy and defect-free by pressure sintering at room temperature.

These new glass SEs begin as fine grained and agglomerated powders as a result of the MCM processing and feature properties and structures that are strongly dependent on the oxygen doping. We have observed that during normal uniaxial pressing at pressures less than 300 MPa, these SEs spontaneously transform into fully dense and microscopically and macroscopically homogeneous smooth glasses that behave as if they had been melt quenched (MQ) to the normal glassy state. Their homogeneous structures appear to be isostructural to glasses of the same composition produced by normal MQ processes. This structural transformation appears to be unique among oxysulfide SEs at the reported oxygen doping levels. We have observed that the formation of the homogenous bulk glassy phase is an essential property of these SEs to create the mechanical, chemical, and electrochemical stability towards Na metals (**Scheme 1c**).

The ternary composition of $\text{Na}_2\text{S}-\text{P}_2\text{S}_5-\text{P}_2\text{O}_5$ reported here has been carefully designed following five rules: first, P_2S_5 with a low melting point is a strong glass former that appears to facilitate the formation

of a structurally homogeneous bulk glass under pressure, which we find is crucial to suppressing the Na dendrites propagation^{17,18}; second, following previous studies of oxysulfide glasses where the added oxygen preferentially forms structure enhancing bridging oxygens (BO), P₂O₅ with stronger chemical bonding of P–O compared to that of P–S can reinforce the glass network¹⁹, thereby boosting the mechanical strength and retarding the known chemical decomposition of pure sulfide SEs^{15,20,21}; third, following our previous observations on binary Na₂S + P₂S₅ glasses^{22,23}, made either by MCM or MQ techniques, maximum Na⁺ ion conductivity was observed at maximum Na₂S concentration; fourth, pure sulfide glasses always exhibit superior Na⁺ ion conductivities over pure oxide glasses²⁴⁻²⁷; and fifth, again following our previous observations²⁸ and those of Hayashi et al.²⁹, that in mixed oxysulfide glasses, the conductivity rapidly increases with small sulfur replacements, < 25 mol.%, but then decreases strongly after this maximum.

In this work, we conducted a systematic characterization of the sodium phosphorous oxysulfide SE, Na₃PS_{4-x}O_x (NPSO), where 0 ≤ x ≤ 0.6, by examining their chemical structures, mechanical properties, chemical stabilities, resistance to Na metal dendrites, and their overall electrochemical performance as measured in Na/SE/Na symmetric cells. Their performance at both reducing and oxidizing potentials was examined by forming and successfully cycling ambient-temperature sodium-sulfur batteries (ATSSBs). We believe these mixed oxysulfide SEs and their unique homogenous defect-free bulk glassy structure produced at relatively low pressures provide a new paradigm in the development of safe, low cost, energy dense and long lifetime ASSSBs.

Results And Discussion

Formation of Chemically Reacted Glasses. The synergistic effects of oxygen additions on the properties of the NPSO SEs were examined on different compositions of x = 0, 0.15, 0.30, 0.60 that were synthesized via the high-energy MCM and systematically characterized. The XRD patterns (Supplementary Fig. S1) show that all the raw materials became amorphous after MCM, as no diffraction peaks of the starting materials were detected. Hayashi et al. and we have observed that unreacted Na₂S and P₂S₅ were observed for MCM times shorter than those used here and that unreacted Na₂S was observed for Na₂S contents higher than those used here.^{22,30} Full chemical reaction between the Na₂S and P₂S₅ and not just amorphization of the starting materials was proven though the chemical spectroscopies, infrared (IR), Raman, nuclear magnetic resonance (NMR), and X-ray photoelectron spectroscopy (XPS). The DSC curves in Supplementary Fig. S2 further reveal that all of the amorphous samples are glassy exhibiting a glass transition (T_g) around 200°C. For the oxysulfide SEs (x > 0), the working range, or the difference between T_g and T_c , becomes larger with increasing oxygen contents, indicating adding oxygen results in greater resistance to crystallization.

While complete understanding of the complex mechano-chemical processes taking place during high-energy MCM are as yet not fully known, it is generally agreed that MCM generates high local

temperatures during the rapid ball to material to wall and ball to material to ball collisions and generates rapid thermal quenching after the collision as the materials are thermalized back to the near room temperature of the reaction vessel. The combination of high local temperature and the rapid quenching are believed to be responsible for the formation of amorphous materials that also exhibit a liquid state formed glassy Tg. However, just as in MQ systems, the quenching rate is not always sufficient to yield a fully amorphous glass and the presence of small amounts of crystalline phases can be detected in some systems, which was recently observed in the $\text{Na}_2\text{S}-\text{P}_2\text{S}_5$ ³¹ and $\text{Li}_2\text{S}-\text{P}_2\text{S}_5$ ³² systems.

To examine in more detail the possible formation of small amounts of fine-grained crystalline phases in the NPSO SEs during the MCM process, high-energy synchrotron XRD patterns were collected and shown in Fig. 1a. All synthesized SEs feature two broad halos superimposed with weak Bragg peaks, indicating that a small number of fine-grained crystalline phases do form and are embedded in the majority of an otherwise glassy matrix. The TEM image and SAED pattern (Supplementary Fig. S3) show that the crystalline phase is tetragonal Na_3PS_4 ($t\text{-Na}_3\text{PS}_4$) with an average particle size of ~ 3 nm. However, as seen in Fig. 1a, when x reaches 0.6, these crystallization processes weaken as evidenced by the fact that the $t\text{-Na}_3\text{PS}_4$ peak has almost disappeared. However, it is now replaced by the appearance of crystalline Na_2S that may arise from incomplete chemical reaction.

The reason for the appearance Na_2S at the higher O substitution was examined by Raman spectroscopy since it is sensitive to sulfur-containing units. As seen in Fig. 1b, the primary feature peak²⁵ centered at 420 cm^{-1} is assigned to the stretching mode of the PS_4 unit, which is a non-bridging sulfur (NBS) unit, identified as P^0 ^{24,30} where the superscript 0 is the number of bridging oxygens (BOs) on this short range order (SRO) unit. The Gaussian fitting of this mode (Supplementary Fig. S4) suggests that with the oxygen incorporation, a small population of the original P^0 units disproportionate into P^1 units (containing one bridging sulfur (BS), e.g. P_2S_7) with the liberation of sodium sulfide ($2\text{P}^0 \rightarrow 2\text{P}^1 + \text{Na}_2\text{S}$)²⁴ to balance charge. This disproportionation reaction is supported by the observation of Na_2S peaks in the synchrotron XRD results. The mode centered at 380 cm^{-1} is assigned to the P_2S_6 unit, which possesses a homopolar P–P bond, that decreases in concentration with the oxygen addition³³. The formation process of the P_2S_6 defect unit generates residual sulfur species (e.g. sulfur element) that show a characteristic Raman mode arising from the –S–S– linkage and occurs at 470 cm^{-1} . As indicated from both Fig. 1a and 1b, except for a small amount of crystalline phases of Na_3PS_4 and Na_2S , which we estimate to be in the range of < 5%, the main composition of the NPSO SEs is glass.

Chemical Short-Range Order. ^{31}P MAS-NMR was used to gain further insights into the glassy phase of these NPSO SEs by examining the local structure around the phosphorus glass forming cation. Deconvolution of the ^{31}P NMR spectra (Fig. 1c) shows that the glass Na_3PS_4 ($x = 0$) is composed mainly of PS_4 (82 ppm) and P_2S_6 (108 ppm) units, which is consistent with the Raman spectra described above. With the incorporation of oxygen, three new peaks attributed to the formation of mixed oxysulfide and oxide units, PS_2O_2 oxysulfide (63 ppm), PSO_3 oxysulfide (32 ppm), and PO_4 oxide (3 ppm) units can be

clearly observed³⁴. The peak for the expected but missing PS_3O oxysulfide units is nearly indiscernible since it has essentially the same chemical shift as the PS_4 units²⁹.

However, following the methods we proposed before^{24,35}, this unit and its relative fraction of all of the SRO units was determined by careful spectral deconvolution and corrected for charge balance among the Na^+ ions and the various $\text{PS}_{4-x}\text{O}_x$ anions. The composition dependence of the population of the various SRO structural units in these oxysulfide NPSO SEs is given in Fig. 1d and shows that as expected the fractions of mixed oxysulfide units dramatically increases with oxygen doping level and become the dominant species when x reaches 0.6. The appearance of $\text{PS}_{4-x}\text{O}_x$ oxysulfide SRO units suggests that the oxygen has been incorporated into the P–S tetrahedra unit, which is expected to improve the chemical stability and mechanical strength of the glass network over that of the pure sulfide SE.

FTIR spectroscopy was further applied to explore the chemical bonding between phosphorus and sulfur and phosphorous and oxygen. The FTIR spectra shown in Fig. 1e can be divided into three sections corresponding to terminal $\text{P}-\text{S}^-$ ($400\text{--}600\text{ cm}^{-1}$), BO $\text{P}-\text{O}-\text{P}$ ($600\text{--}950\text{ cm}^{-1}$) and terminal non-bridging oxygens (NBOs) $\text{P}-\text{O}^-$ or $\text{P}=\text{O}$ ($950\text{--}1200\text{ cm}^{-1}$) modes, respectively^{36,37}. Detailed peak assignments are listed in Supplementary Table S1. It is evident that oxygen incorporation into the glass matrix leads to a slightly increased fractions of $\text{P}-\text{O}^-$ and $\text{P}=\text{O}$ bonds and a particularly significant increase in the fraction BO $\text{P}-\text{O}-\text{P}$ bonds, where the O atom is bridging between two phosphorus atoms. Further evidence of the formation of BOs on adding oxygen to Na_3PS_4 can be found in O 1s XPS spectra (Fig. 1f), where the BO with the binding energy of 532.5 eV^{38,39} accounts for the higher fraction of the oxygen (NBOs) for larger x values in NPSO SEs. Spectral deconvolution of $\text{Na}_3\text{PS}_{3.4}\text{O}_{0.6}$, for example, shows that more than 90% of the added oxygen atoms are present as BOs in the glass. This behavior is completely consistent by our previous work⁴⁰ where in a similar $\text{Li}_2\text{GeS}_{4-x}\text{O}_x$ glass system, the added oxygen was also found to preferentially replace S in the BS positions until all of the BS were eliminated. It was not until there were no more BS to replace did the oxygen form NBOs. The results here for the NPSO series reveal a more complex mechanism for the added oxygen to form BO because in the present system, there are no BSs to begin with. Hence, the added O forces the formation of the disproportionation reactions described above. To maintain charge balance in the series, the formation of a BO requires the formation of “free” Na_2S in direct proportion to the amount of O added. While overall charge balance appears to be maintained in this system, the formation of BOs through the addition of O also forms increasing chain units in the form of P^1 units. Kmiec et al. has observed this same behavior in the slightly lower modifier $\text{Na}_4\text{P}_2\text{S}_{7-x}\text{O}_x$ system³⁵. Using the SRO composition map similar to Fig. 1d, Kmiec calculated the average chain length that forms through the formation of BOs in these systems. The network chain connection of the structural units creates an interconnected glass network that produces glasses with increasing packing densities, mechanical moduli, and stronger chemical bonding that improves the chemical stability of SEs.

Homogeneous Glass with Improved Mechanical Properties. A defect-free and mechanically robust SE is a prerequisite for successfully cycling with Na metal anodes¹¹. Consequently, the morphological structure and the mechanical properties of NPSO SEs were investigated. For comparison, the widely studied heat-treated Na_3PS_4 glass-ceramic SE (HT- Na_3PS_4) was also studied^{25,41}. Obvious pores and grain boundaries are clearly observed in the SEM images of pelletized HT- Na_3PS_4 (Fig. 2a–b). These surface defects (pores and grain boundaries) are believed to induce dendrite formation, subsequent dendrite propagation^{42–44}, and eventual short-circuit through the SE, as demonstrated in Supplementary Fig. S5. Na_3PS_4 glass SE, however, shows fewer structural pores compared to HT- Na_3PS_4 . In sharp contrast to both of these SEs, the surface of the NPSO glass SE appears to be absent of pores from the surface through to the interior. To the best of our knowledge, this defect-free fully dense glassy morphology induced by simple low-cost room temperature uniaxial pressing is observed here for the first time in any SE fabricated by simple cold-pressing. Such a perfect morphology is presumably closely related to the outstanding formability of NPSO. As shown in Fig. 2b and Fig. S5, this phase is nearly fully densified at a pressure as low as 150 MPa. In comparison, Na_3PS_4 glass and HT- Na_3PS_4 couldn't achieve similar relative density even when much higher pressures were applied during cold-pressing. The excellent formability of these oxysulfide SEs is attributed to the synergistic effects of mixed P_2S_5 and P_2O_5 glass formers, which not only build a close-packed glass network with abundant BO units but also facilitate the local sintering process of the powders as demonstrated by more interparticle adhesion and necking compared to the pure sulfide SEs particles(Supplementary Fig. S7). Overall, for oxysulfide SEs, their unique formability and defect-free structure will undoubtedly enhance their mechanical strengths and reduce the likelihood of dendrite-induced short-circuit when using Na metal anode, as described in Scheme 1a.

To quantify the mechanical properties of SEs, two critical parameters: Young's modulus E and hardness H were measured using nano-indentation technique⁴⁵. Typical load-displacement curves in Fig. 2 and Supplementary Fig. S8 show that the HT- Na_3PS_4 pellet experiences a sudden increase of indenter penetration during the loading process, which is not found in glassy NPSO SEs. This is referred to as “pop-in” and is associated with the generation of a crack^{45,46}. This behavior indicates that the HT- Na_3PS_4 SE is more brittle than the glassy counterparts. Such cracking of course is certainly unfavorable for the preparation and practical application of SEs. Further, benefiting from the homogeneous property of the glassy materials, the NPSO SEs display very small standard deviations for E and H as seen in the bar chart in Fig. 2d. Moreover, the oxygen doping results in an increase of E and H of SEs, which supports the observation that oxygen doping produces more BO units in the glass network, thus providing more robust mechanical properties. The E and H of $\text{Na}_3\text{PS}_{3.4}\text{O}_{0.6}$ glass were measured to be 20.9 ± 0.7 GPa and 1.0 ± 0.1 GPa, respectively, which is the highest among the NPSO series and even higher than those of the reported sulfide-based Li-ion and Na-ion SEs prepared by hot-pressing^{18,47,48}. Assuming that Poisson's ratio ν is ca. 0.3 according to the study from Sakuda et al.⁴⁹, the shear modulus G of $\text{Na}_3\text{PS}_{3.4}\text{O}_{0.6}$ glass is ca. 8.0 ± 0.3 GPa, which is believed to be sufficient to suppress dendritic penetration of Na metal as predicted by the Monroe and Newman criterion⁵⁰.

Electrochemically Stable SEs Against Na Metal. As described above, the chemical and electrochemical stability of SEs against Na metal anodes is critically important for developing high-performance ASSSBs and for this reason we have examined the Na – NPSO interface using time-dependent electrochemical impedance spectroscopy (EIS) and XPS. Na/NPSO/Na symmetric cells were fabricated to monitor the evolution of the EIS spectra and the area specific resistance (ASR) over 5 hours resting time and this is shown in Fig. 3a and Supplementary Fig. S9, respectively. The obtained EIS spectra can be divided into three semicircle regions⁵¹ and the fitting parameters are listed in Supplementary Table S2. The high-frequency semicircle represents the combined bulk and grain boundary resistance and capacitance ($R_b + R_{gb}, C_b + R_{gb}$) of the SEs; the mid-frequency semicircle with the characteristic capacitance of $10^{-6} \sim 10^{-7}$ F arises from the interfacial resistance and capacitance (R_i, C_i) between Na and SE⁵²; and the low-frequency one corresponds to the charge-transfer resistance and capacitance(R_{ct}, C_{ct}). As seen from Table S2 and Fig. S9, the added oxygen has a positive effect on improving the SEs' chemical stability against Na metal. Not only do the R_i and R_{ct} resistances decrease significantly, but their increase after contact with Na metal becomes negligible. Further, Fig. S9 shows that the ASR becomes less significant when more oxygen is doped. Indeed, it is noteworthy that for the $\text{Na}_3\text{PS}_{3.4}\text{O}_{0.6}$ SE, not only does the ASR increase essentially vanish, it further presents a negligible change of R_b and R_{ct} , but also indistinguishable R_i , suggesting an intimate and ohmic contact that forms a stable interface between $\text{Na}_3\text{PS}_{3.4}\text{O}_{0.6}$ and Na. In contrast, all of the other SEs display a R_i varying with time, indicating an unstable Na – SE interface.

To identify the interphase composition that apparently grows with time for the $x \neq 0.6$ glassy NPSO SEs, Na metal was detached from the symmetric cells and the surface of SEs was probed by the XPS. Compared to the surfaces of the pristine SEs (Supplementary Fig. S10), Fig. 3 shows that the surfaces of the $\text{Na}_3\text{PS}_{4-x}\text{O}_x$, $x = 0, 0.15$, and 0.3 , SEs exhibit two new pairs of doublets for P 2p spectra and S 2p spectra at lower bonding energy after contacting with Na metal. These new pairs of doublets correspond to the reduced phosphide and sulfide species, respectively, and indicates that these electrolytes have been reduced by Na metal. According to the theoretical calculation from Tian et al.¹² and the experimental study from Wenzel et al.¹³, these reduced species are Na_2S and Na_3P , respectively, the latter of which is a mixed ionic and electronic conductor that can cause continuous reduction of the electrolyte. Thus, for these SEs an unstable interphase grows between the Na anode and SE, impeding the Na stripping/plating process. Similar phenomena have been observed in other pure sulfides and selenides, e.g. Na_3PS_4 , Na_3SbS_4 , Na_3PSe_4 , and while they all have high ionic conductivities, their propensity to form these unstable interphases make them unsuitable in Na-metal batteries¹⁴.

In contrast, Fig. 3 shows that these same XPS signals from these reduced species are nearly indiscernible above the baseline noise in the S2p and P2p spectra for the $\text{Na}_3\text{PS}_{2.4}\text{O}_{0.6}$ SE, validating the negligible ASR increase from EIS measurement. To our knowledge, this is the first sulfide-based defect-free fully glassy SE that forms a stable non-reacting interphase directly against Na metal.¹⁶ We assert here that the outstanding chemical stability of $\text{Na}_3\text{PS}_{3.4}\text{O}_{0.6}$ in contact with Na metal is contributed by: first,

$\text{Na}_3\text{PS}_{3.4}\text{O}_{0.6}$ has a more robust glass network than the other SEs due to the existence of more BOs units which have higher electronic binding energies; second, and in a similar way in comparing NBO to NBS moieties, oxide and oxysulfide units also have higher electronic binding energies than pure sulfide units; third, even if NBOs and BOs do react with Na metal, the terminal oxygen in $\text{P} - \text{O}^-$ may react with Na metal and form a thin electronic insulating interphase (Na_2O) as suggested by Gao et al. for solid-state electrolytes⁵³ and by Seh et al. for liquid electrolytes⁵⁴.

Electrochemically Stable and High Na^+ Ion Conductivity Tri-Layer Composite SEs. Figure 4a shows the temperature-dependence of the Na^+ ionic conductivities that were obtained from the Nyquist plots (Supplementary Fig. S11) for the $\text{Na}_3\text{PS}_{4-x}\text{O}_x$, $x = 0, 0.15, 0.30, 0.60$. From Supplementary Fig. S12, it is intriguing that the ionic conductivities exhibit a 6-fold increase with the initial addition of oxygen, $x = 0.15$, rendering the conductivity of the $\text{Na}_3\text{PS}_{3.85}\text{O}_{0.15}$ SE as high as $2.7 \times 10^{-4} \text{ S cm}^{-1}$ and activation energy as low as 41.5 kJ mol^{-1} . This anomalous increase in the ionic conductivity may be associated with two distinctly different features of the effects of the addition of oxygen to the base Na_3PS_4 glassy SE. First, when we doped oxygen into the comparable $\text{Li}_2\text{GeS}_{2-x}\text{O}_x$ glassy SE in a previous study⁴⁰, we observed that the added oxygen increased the free volume available to the mobile Li^+ ion for conduction. This led to an increase of the ‘doorway’ radius, r_D , between Li^+ ion sites, thereby lowering the overall activation energy and increasing the conductivity²⁸. While these two systems are different, the compositional similarity and the similar sharp increase in the conductivity suggest a similar underlying mechanism. Second, as evidenced in the synchrotron XRD data, Fig. 1a., the existence of highly conductive *t*- Na_3PS_4 crystalline phase²⁵ may add a second highly conductive parallel phase, although less than 5% fraction, that gives rise to the overall higher conductivity.

Further additions of oxygen monotonically increase the activation energy thereby decreasing the conductivity. Consistent with our previous studies,²⁸ the added oxygen collapses the structure thereby decreasing the free volume available for conduction and increasing the activation energy through the formation of further BO units. Further decreasing the conductivity is the formation of a very poorly conductive Na_2S phase formed through the disproportionation reaction described above. As a result, the $\text{Na}_3\text{PS}_{3.4}\text{O}_{0.6}$ SE shows a lower conductivity of $8.2 \times 10^{-5} \text{ S cm}^{-1}$ at 60°C . Furthermore, it has been recently reported that high electronic conductivity of SEs originating from internal defects (cracks, pores, grain boundaries) is responsible for Li dendrite formation and growth in SEs^{55,56}. Figure 4b compares the electron conductivity of $\text{Na}_3\text{PS}_{3.4}\text{O}_{0.6}$, Na_3PS_4 and HT- Na_3PS_4 measured by two ion-blocking electrodes at 60°C . $\text{Na}_3\text{PS}_{3.4}\text{O}_{0.6}$ shows two orders of magnitude lower electronic conductivity than that of HT- Na_3PS_4 , supporting the unique defect-free microstructure of oxysulfide SE which will undoubtedly reduce the likelihood of dendrite-induced short-circuit.

However, the superb formability of the $\text{Na}_3\text{PS}_{3.4}\text{O}_{0.6}$ SE can provide a means to fabricate a thin SE layer, the resistance of which could be very low. An ideal SE for ASSSBs requires both high ionic conductivity and excellent mechanical and chemical stability. To create such an SE, therefore, a tri-layer architecture

with the most ionically conductive $\text{Na}_3\text{PS}_{3.85}\text{O}_{0.15}$ in the middle and the most mechanically and chemically stable $\text{Na}_3\text{PS}_{3.4}\text{O}_{0.6}$ on the outside was designed and is shown in the inset of Fig. 4c. From the SEM images shown in Supplementary Fig. S13, an entirely all-glass SE separator without any discernible voids or grain boundaries was attained owing to the excellent formability and densification. The cyclability of the tri-layer electrolyte was studied in a symmetric $\text{Na}|\text{trilayer-SE}|\text{Na}$ cell using gradient-current and constant-current tests, as shown in Fig. 4c and Fig. 4d–e, respectively. As seen in Fig. 4c, the voltage profile of the tri-layer separator shows an ohmic response, $V = IR$; however, sudden voltage spikes occur when the current exceeded 2.3 mA cm^{-2} , which was determined to be the critical current density (CCD) for the tri-layer SE. 2.3 mA cm^{-2} is the highest reported CCD value for sulfide-based Na-ion SEs, which is also comparable to the state-of-art CCD value of Li-ion based sulfide SEs. The increased capability of the oxysulfide SEs to resist Na dendrite formation and penetration is attributed to their homogeneous and porosity-free structure and robust mechanical properties. These observations agree with Porz et al.'s¹¹ conclusions on the failure mechanisms of SEs toward a metal anode where they observed that Griffith's flaws in the surface of the SEs drive dendritic growth and propagation through SEs.

Figure 4d and 4e show that a symmetric cell with a tri-layer electrolyte can stably cycle for several hundred hours without short-circuiting at current densities of 0.2 mA cm^{-2} and 0.5 mA cm^{-2} , respectively. The inserts to Figs. 4d and 4e show that very flat voltage profiles are observed at each cycle over the range of time that the cell was cycled. This behavior indicates that the Na plating and stripping processes are very stable at the $\text{Na}_3\text{PS}_{3.4}\text{O}_{0.6}-\text{Na}$ interface, consistent with the discussion above. As seen, the charge-transfer resistance for $\text{Na}_3\text{PS}_{3.4}\text{O}_{0.6}-\text{Na}$ is only $\sim 10 \Omega \cdot \text{cm}^2$. Fig. S14 compares this work and some of the state of art reports on $\text{Na}|\text{SEs}|\text{Na}$ symmetric cells for different categories of reported Na-ion conducting SEs. Three key parameters, which determine the energy density, power density, and cycling life of practical full cells are shown in this figure; the capacity of Na metal plated per cycle (area of the circle), current density, and cycling time. It is clear from this figure that the composite tri-layer oxysulfide SE developed in this work significantly extends the cycle time and current density performance for SEs cycling Na in symmetric cells. In particular, our composite tri-layer SE sets new standards for higher current density and longer cycling times in ASSSBs.

It has been shown above that the $\text{Na}_3\text{PS}_{3.4}\text{O}_{0.6}$ SE can be combined with $\text{Na}_3\text{PS}_{3.85}\text{O}_{0.15}$ to create a stable all-glass separator. In a similar manner, using the tri-layer architecture, $\text{Na}_3\text{PS}_{2.4}\text{O}_{0.6}$ can be used for protecting other highly conducting but chemically unstable (against Na metal) SEs such as glass-ceramics, e.g. HT- Na_3PS_4 , or ceramics, e.g. Na_3SbS_4 . An example of this is shown in Supplementary Fig. S15 for $\text{Na}_3\text{PS}_{3.4}\text{O}_{0.6}|\text{HT-Na}_3\text{PS}_4|\text{Na}_3\text{PS}_{3.4}\text{O}_{0.6}$. Due to the ease at which the $\text{Na}_3\text{PS}_{3.4}\text{O}_{0.6}$ SE deforms under pressure to form a homogeneous interface, excellent interfacial contact can be achieved between these two SEs. Furthermore, Fig. S15 shows that the $\text{Na}|\text{trilayer-SE}|\text{Na}$ symmetric cells also show very stable Na plating/stripping profiles at 0.2 mA cm^{-2} for up to 500 h and up to 240 h at 0.5 mA cm^{-2} .

All Solid-State Na–S Full Cells. The excellent $\text{Na}_3\text{PS}_{2.4}\text{O}_{0.6}$ –Na stability enables the fabrication of ASSSBs, of which the ambient-temperature Na–S battery is one of the most promising because of its very low cost and high specific energy. On the basis of the above study that demonstrated the stability of the tri-layer SE in a Na metal symmetric cell, a Na–S battery having the architecture of S–Ketjen Black (KB)– $\text{Na}_3\text{PS}_{3.85}\text{O}_{0.15}$ | $\text{Na}_3\text{PS}_{3.85}\text{O}_{0.15}$ | $\text{Na}_3\text{PS}_{3.4}\text{O}_{0.6}$ |Na was designed and tested at 60°C. Notice here, in the full cell configuration, the second layer of $\text{Na}_3\text{PS}_{3.4}\text{O}_{0.6}$ on the cathode side is not needed because CV measurements, see Fig. S16, shows that the higher conducting $\text{Na}_3\text{PS}_{3.85}\text{O}_{0.15}$ SE is stable to the oxidizing potentials of 3.3 V for a sulfur cathode. For this reason, the SE separator could be simplified to a bi-layer structure of | $\text{Na}_3\text{PS}_{3.85}\text{O}_{0.15}$ | $\text{Na}_3\text{PS}_{3.4}\text{O}_{0.6}$ |, the slightly poorer conducting but very stable $\text{Na}_3\text{PS}_{3.4}\text{O}_{0.6}$ SE was used to create a stable interface to Na metal.

Figure 5a shows the voltage profiles for the cell operated within the voltage window of 1.0 to 3.0 V. The cell shows a high initial discharge capacity of 1280 mAh g⁻¹, which is 76% of the theoretical capacity of sulfur (Na→ Na_2S : 1675 mAh g⁻¹) and much higher than that, 558 mAh g⁻¹, of the conventional high-temperature Na–S battery⁵⁷. This is because the Na–S battery described here is an all-solid-state system that does not have the discharge limitation of Na→ Na_2S_4 that the high-temperature Na–S battery exhibits. The first cycle coulombic efficiency is 92%, indicating that the polysulfide shuttle phenomenon commonly found in a liquid electrolyte-based cell is not observed in the current system. The cell then improves to ~100% coulombic efficiency after first initial five cycles. Upon further cycling, the reversible capacity stabilizes at about 1000 mAh g⁻¹ after 40 cycles with capacity retention more than 80% (Fig. 5b). These values are significantly better than those of the reported Na–S batteries using oxide or polymer SEs and Table S3 summarizes these previously reported solid-state Na–S batteries^{58–65} operated near ambient temperature in comparison to that reported here. The discharge voltage profile shows two plateaus located at 1.9 V and 1.25 V vs. Na^+/Na with a single slope in between. The average discharging potential is 1.42 V, which is higher than those of other pure sulfide SE-based Na–S batteries that use $\text{Na}_{15}\text{Sn}_4$ or Na_3Sb alloy anodes.

The rate capability of our Na–S battery was evaluated by examining the capacity by cycling at increasing current densities. As seen in the Supplementary Fig. S16, the cell can deliver specific capacities of 1116, 908 and 574 mAh g⁻¹ at current densities of 0.10, 0.20 and 0.35 mA cm⁻², respectively. After the current was returned to 0.10 mA cm⁻², the cell capacity also reverted to a value close to the original one and the cell cycled stably for another 150 cycles (Fig. 5c). The significantly improved Na–S battery cycling performance is attributed to the excellent interface stability, which enables Na metal to stably plate/strip at high rates, the superior formability property of oxysulfide SEs, which ensures the consistently good contact with sulfur and carbon during cycling, and the overall solid nature of the SEs that completely stops any polysulfide shuttle between the anode and the cathode. Therefore, the oxysulfide-based Na–S battery described here shows the highest specific energy density among all currently reported all-solid-state Na–S batteries (Fig. 5d). For these reasons, we believe these oxysulfide composite SEs may offer

an entirely new and successful approach to the development of low cost, high energy density, safe, and high cycle life Na-based solid-state batteries.

Conclusions

A new class of oxysulfide glass SEs with combined advantages of sulfide SEs and oxide SEs was successfully synthesized and systematically investigated in both symmetric and full cell configurations. Compared with pure sulfide SEs, oxygen-doped oxysulfide SEs show much stronger and denser glass networks due to the formation of higher concentrations of oxide and oxysulfide units with BO characteristics. In addition, it is found that while the addition of oxygen increases the mechanical strength of the glassy SE, it also causes these oxysulfide SEs to exhibit the never before seen capability of pressure induced homogenization of the glassy powder starting materials into continuous near flawless glass microstructure. This dramatically improved formability causes the as-formed homogeneous oxysulfide SEs to have significantly higher mechanical strength, lower electronic conductivity, and dramatically increased chemical stability towards Na metal. A defect-free tri-layer composite SE with $\text{Na}_3\text{PS}_{3.4}\text{O}_{0.6}|\text{Na}_3\text{PS}_{3.85}\text{O}_{0.15}|\text{Na}_3\text{PS}_{3.4}\text{O}_{0.6}$ can demonstrate a critical current density of up to 2.3 mA cm^{-2} , the highest reported CCD value for Na-ion sulfide SEs, and cycle stably at 0.2 mA cm^{-2} for up to 500 h. Using a composite oxysulfide bi-layer SE, full Na–S cells were fabricated and were shown to provide the highest specific energy among all known solid-state Na–S systems to date. These new oxysulfide SEs and the tri-layer composite SEs that they enable, may provide a very promising avenue of research towards the development of new glass electrolytes for high energy, safe, low cost and long cycle life solid-state batteries in general and all-solid-state Na–S batteries for energy storage devices.

Methods

Synthesis of NPSO SEs. Na_2S , P_2S_5 , and P_2O_5 (Sigma-Aldrich, 99%) were used as the raw materials without further purification. The $\text{Na}_3\text{PS}_{4-x}\text{O}_x$ ($x = 0.15, 0.30$ and 0.60) SEs were prepared by high-energy planetary ball milling (MTI, MSK-SFM-1). Typically, 2 g mixtures of appropriate amounts of Na_2S , P_2S_5 and P_2O_5 powders were milled in an Argon-protected stainless steel jar containing stainless steel milling balls at 500 rpm for 3 h to obtain the amorphous SEs. Note different milling media and milling time were used in this work compared to Lazer et al.¹⁶, where ZrO_2 -based milling media and 20 h of milling were used. The pure sulfide $x = 0$ SE was synthesized by ball-milling raw materials in the agate jar at 500 rpm for 20 h. The Na_3PS_4 glass-ceramic SE, HT- Na_3PS_4 , was obtained from the glassy Na_3PS_4 by heating under vacuum at 260°C for 2 h.

Materials characterizations of NPSO SEs. Since oxysulfide SEs are sensitive to air and moisture, all of the characterizations were conducted under Argon protection. Lab-based X-ray diffraction (XRD) and synchrotron XRD patterns were collected using a Rigaku MiniFlex 600 with $\text{Cu K}\alpha$ radiation ($\lambda = 1.5418 \text{ \AA}$) and Beamline 11-ID-C at Advanced Photon Source with X-ray wavelength of 0.1173 \AA , respectively, to

determine the crystallinity and the identity of the crystalline phases in the various SEs. The thermal behavior of the SEs powders was examined using differential scanning calorimetry, DSC, TA Instruments Q2000, using nitrogen as the carrier gas. The sample was placed in the Tzero aluminum pan and hermetically crimp-sealed inside the Argon-filled glove box. The DSC measurements were carried out at a heating rate of $20^{\circ}\text{C min}^{-1}$ from 50°C to 400°C . A Renishaw inVia Raman spectrometer employing a 488 nm Ar⁺ laser and 10 mW of power was used to collect the Raman spectra from 200 to 700 cm^{-1} . SE powders were placed into a small plastic sample holder inside the glove box and covered with transparent tape to prevent exposure to air during data collection. Infrared (IR) spectra were acquired on a Bruker IFS 66 v/s vacuum IR spectrometer in the range of $400 - 1200\text{ cm}^{-1}$ using a KBr beamsplitter. During the test, the spectrometer optical bench was held under vacuum to protect the samples from moisture and air. The IR spectra of the samples were taken by diluting the finely ground glass and glass-ceramic powders to ~ 2% in finely ground and carefully dried CsI and then pressed into small pellets. ³¹P Solid-state Magic Angle Spinning Nuclear Magnetic Resonance (MAS NMR) spectra were collected using a JEOL ECA-500 NMR spectrometer. SE powders were packed into an alumina spinner with a sealant in an Argon-filled glove box. Spectra were collected using a $4.25\text{ }\mu\text{s}$, 60° pulse length, and a 200 s recycle delay with the spinning speed of 20 kHz. Chemical shifts were externally referenced to NaH₂PO₄. The elastic modulus E, hardness H, and interfacial fracture toughness K_c were measured using the same method as we reported before⁴⁵. Briefly, E and H values were measured using a G200 Keysight nanoindenter with a Berkovich indenter using the Oliver-Pharr method on samples inside an argon-filled glove box to avoid moisture and air contaminations. Indentations with a maximum indentation load of 1 mN were pressed on different spots of the SE surfaces to ensure the convergence of the measured results. The load-displacement curves up to the pellet cracking were recorded during the tests. Morphologies of the SEs powders, as well as the surface and cross-section of the densified pellets, were observed using a Gemini LEO 1525 scanning electron microscope (SEM). Nanocrystals embedded in the glass SE were confirmed using a JEOL 2100F transmission electron microscope (TEM). The X-ray photoelectron spectroscopy (XPS) spectra were collected using a Physical Electronics PHI 5700 on the SEs pellets using a monochromatic Mg Ka X-ray source. The XPS signals were corrected relative to the C 1s signal (284.8 eV) and fitted using the XPSPEAK41 software. The relative density of the SEs was defined as $\rho_{\text{bulk}}/\rho_{\text{true}}$, where ρ_{bulk} is the bulk density and ρ_{true} is the true density of powders according to Nose et al.'s report¹⁸. ρ_{true} for Na₃PS₄ and Na₃PS_{3.4}O_{0.6} were 2.00 g cm^{-3} ¹⁸ and 2.28 g cm^{-3} , respectively.

Electrochemical characterizations of SEs. The temperature-dependent ionic conductivities of the pelletized SEs were measured from 25°C to 90°C using alternating current impedance method (frequency: 1 MHz–0.1 Hz, amplitude: 5 mV) on a VMP3, Bio-Logic Co. electrochemical workstation. Before the measurement, the SEs powders were cold-pressed in a polyetheretherketone (PEEK) test cell die ($\phi = 13$ mm) under a pressure of 450 MPa and then co-pressed with 20 mg nano-copper powders (Sigma-Aldrich, 40–60 nm, $\geq 99.5\%$) as the electrodes under a pressure of 200 MPa. Chemical stability of the SEs towards Na metal was studied by monitoring the impedance change vs. time of the symmetric cell

$\text{Na}|\text{SE}|\text{Na}$, which was assembled by attaching two same pieces of Na metal foils ($\sim 100 \mu\text{m}$ in thickness) on both sides of the SEs. For the fabrication of tri-layer electrolytes, ~ 150 mg of $\text{Na}_3\text{PS}_{3.85}\text{O}_{0.15}$ glass or Na_3PS_4 glass-ceramic SE powders were cold-pressed at 75 MPa; then ~ 25 mg of $\text{Na}_3\text{PS}_{3.4}\text{O}_{0.6}$ glass powders were evenly distributed on both sides of as-pressed pellet; finally the three layers were co-compressed at 450 MPa. After attaching Na metal foils onto the tri-layer electrolyte, Na plating/stripping test was conducted under galvanostatic mode.

Since $\text{Na}_3\text{PS}_{3.85}\text{O}_{0.15}$ is the most conductive among the NPSO SEs and Ketjen black carbon (surface area of $1400 \text{ m}^2 \text{ g}^{-1}$), they were chosen to blend with sulfur to create both fast ionic and electronic pathways for the sulfur active material in the composite cathode. The all-solid-state Na metal-sulfur batteries were fabricated using a $\text{Na}_3\text{PS}_{3.85}\text{O}_{0.15}|\text{Na}_3\text{PS}_{3.4}\text{O}_{0.6}$ bi-layer electrolyte, sulfur-Ketjen black- $\text{Na}_3\text{PS}_{3.85}\text{O}_{0.15}$ composite and Na metal as the separator, cathode, and anode, respectively. In detail, sulfur (99.5%, Alfa Aesar) and Ketjen black (EC-600JD, AkzoNobel) powders with a weight ratio of 1:1 were ball-milled in an agate jar at a rotation speed of 500 rpm for 20 h to obtain a sulfur/KB nanocomposite, which was then milled with $\text{Na}_3\text{PS}_{3.85}\text{O}_{0.15}$ powders at a rotation speed of 350 rpm for 30 min. The weight ratio of sulfur: KB: $\text{Na}_3\text{PS}_{3.85}\text{O}_{0.15}$ composite cathode is 2:2:6. 150 mg $\text{Na}_3\text{PS}_{3.85}\text{O}_{0.15}$ electrolyte powders were firstly pressed at 75 MPa into a pellet, of which one side was then uniformly covered with 20 mg $\text{Na}_3\text{PS}_{3.4}\text{O}_{0.6}$ powders and ~ 1 mg composite cathode powders. Bulk-type all-solid-state Na–S batteries were fabricated after co-pressing at 450 MPa and attaching a piece of Na metal foil. Galvanostatic tests were performed in the potential range of 1.0 to 3.0 V vs. Na at different current densities from 0.05 to 0.35 mA cm^{-2} . All the electrochemical tests were conducted at 60°C .

Data Availability

The data that support the plots within this paper and other findings of this study are available from the corresponding authors upon reasonable request.

Declarations

Acknowledgements

Y.Y. and S. W. M. acknowledge the funding support from the U.S. Department of Energy's Advanced Research Projects Agency-Energy (ARPA-E) (Award number DE-AR0000654). Y.Y. also acknowledges the support of Scialog: Advanced Energy Storage collaborative award from Research Corporation of Science Advancement (Award number 27110). This research used resources of the Advanced Photon Source, a U.S. Department of Energy (DOE) Office of Science User Facility operated for the DOE Office of Science by Argonne National Laboratory under Contract No. DE-AC02-06CH11357.

Author contributions

X.C., S.W.M, and Y.Y. proposed the research. X.C. synthesized the materials, assembled the batteries and performed the electrochemical characterizations. Y.Z. and L.W. carried out the lab-based XRD and synchrotron XRD measurements. S.K. and Y.Z. performed the Raman, NMR, FTIR and DSC measurements. F.H., H.D. conducted XPS characterizations and spectra fitting. K.Z. and R.X. designed and performed the mechanical measurements. L.Z. and L.G. repeated the NPSO synthesis and electrochemical tests. X.C., Y.Z., and F.H. co-wrote the first draft with inputs from all other co-authors. S.W.M, S.K., and Y.Y. revised and finalized the manuscript.

Conflict of Interests

Y.Y. and X.C. have filed a US Patent Application 202106678A. Y.Y. is co-founder of LiBeyond LLC.

References

1. Dunn, B., Kamath, H. & Tarascon, J.-M. Electrical Energy Storage for the Grid: A Battery of Choices. *Science* **334**, 928–935, doi:10.1126/science.1212741 (2011).
2. Tarascon, J. M. & Armand, M. Issues and challenges facing rechargeable lithium batteries. *Nature* **414**, 359, doi:10.1038/35104644 (2001).
3. Janek, J. & Zeier, W. G. A solid future for battery development. *Nat. Energy* **1**, 16141, doi:10.1038/nenergy.2016.141 (2016).
4. Zhao, C. *et al.* Solid-State Sodium Batteries. *Adv. Energy Mater.* **0**, 1703012, doi:10.1002/aenm.201703012 (2018).
5. Zhang, Z. *et al.* New horizons for inorganic solid state ion conductors. *Energy Environ. Sci.* **11**, 1945–1976, doi:10.1039/C8EE01053F (2018).
6. Wen, Z., Hu, Y., Wu, X., Han, J. & Gu, Z. Main Challenges for High Performance NAS Battery: Materials and Interfaces. *Adv. Funct. Mater.* **23**, 1005–1018, doi:10.1002/adfm.201200473 (2013).
7. Wang, Y. X. *et al.* Room-Temperature Sodium-Sulfur Batteries: A Comprehensive Review on Research Progress and Cell Chemistry. *Adv. Energy Mater.* **7**, 1602829, doi:10.1002/aenm.201602829 (2017).
8. Kim, S. M. *et al.* Influence of Carbon Coating on Beta-Alumina Membrane for Sodium-Nickel Chloride Battery. *Bull. Korean Chem. Soc.* **36**, 2869–2874, doi:10.1002/bkcs.10584 (2015).
9. Zhou, W., Li, Y., Xin, S. & Goodenough, J. B. Rechargeable Sodium All-Solid-State Battery. *ACS Cent. Sci.* **3**, 52–57, doi:10.1021/acscentsci.6b00321 (2017).
10. Nikolaev, Y. V., Vybyvanets, V. I., Belousenko, A. P., Dzalandinov, D. N. & Fedorova, V. N. in *IECEC 96. Proceedings of the 31st Intersociety Energy Conversion Engineering Conference*. 1191–1194 vol.1192.
11. Porz, L. *et al.* Mechanism of Lithium Metal Penetration through Inorganic Solid Electrolytes. *Adv. Energy Mater.* **7**, 1701003, doi:10.1002/aenm.201701003 (2017).
12. Tian, Y. *et al.* Compatibility issues between electrodes and electrolytes in solid-state batteries. *Energy Environ. Sci.* **10**, 1150–1166, doi:10.1039/c7ee00534b (2017).

13. Wenzel, S. *et al.* Interfacial Reactivity Benchmarking of the Sodium Ion Conductors Na_3PS_4 and Sodium β -Alumina for Protected Sodium Metal Anodes and Sodium All-Solid-State Batteries. *ACS Appl. Mater. Interfaces* **8**, 28216–28224, doi:10.1021/acsami.6b10119 (2016).
14. Wu, E. A. *et al.* New Insights into the Interphase between the Na Metal Anode and Sulfide Solid-State Electrolytes: A Joint Experimental and Computational Study. *ACS Appl. Mater. Interfaces* **10**, 10076–10086, doi:10.1021/acsami.7b19037 (2018).
15. Tang, H. *et al.* Probing Solid-Solid Interfacial Reactions in All-Solid-State Sodium-Ion Batteries with First-Principles Calculations. *Chem. Mater.* **30**, 163–173, doi:10.1021/acs.chemmater.7b04096 (2018).
16. Lazar, M., Kmiec, S., Joyce, A. & Martin, S. W. Investigations into Reactions between Sodium Metal and $\text{Na}_3\text{PS}_{4-x}\text{O}_x$ Solid-State Electrolytes: Enhanced Stability of the $\text{Na}_3\text{PS}_3\text{O}$ Solid-State Electrolyte. *ACS Appl. Energy Mater.* **3**, 11559–11569, doi:10.1021/acsaeem.0c00914 (2020).
17. Hudgens, J. J. & Martin, S. W. Glass Transition and Infrared Spectra of Low-Alkali, Anhydrous Lithium Phosphate Glasses. *J. Am. Ceram. Soc.* **76**, 1691–1696, doi:<https://doi.org/10.1111/j.1151-2916.1993.tb06636.x> (1993).
18. Nose, M., Kato, A., Sakuda, A., Hayashi, A. & Tatsumisago, M. Evaluation of mechanical properties of $\text{Na}_2\text{S-P}_2\text{S}_5$ sulfide glass electrolytes. *J. Mater. Chem. A* **3**, 22061–22065, doi:10.1039/c5ta05590c (2015).
19. Holzwarth, N. A. W., Lepley, N. D. & Du, Y. A. Computer modeling of lithium phosphate and thiophosphate electrolyte materials. *J. Power Sources* **196**, 6870–6876, doi:<https://doi.org/10.1016/j.jpowsour.2010.08.042> (2011).
20. Zhu, Y., He, X. & Mo, Y. Origin of Outstanding Stability in the Lithium Solid Electrolyte Materials: Insights from Thermodynamic Analyses Based on First-Principles Calculations. *ACS Appl. Mater. Interfaces* **7**, 23685–23693, doi:10.1021/acsami.5b07517 (2015).
21. Han, F., Zhu, Y., He, X., Mo, Y. & Wang, C. Electrochemical Stability of $\text{Li}_{10}\text{GeP}_2\text{S}_{12}$ and $\text{Li}_7\text{La}_3\text{Zr}_2\text{O}_{12}$ Solid Electrolytes. *Adv. Energy Mater.* **6**, 1501590, doi:10.1002/aenm.201501590 (2016).
22. Berbano, S. S., Seo, I., Bischoff, C. M., Schuller, K. E. & Martin, S. W. Formation and structure of $\text{Na}_2\text{S} + \text{P}_2\text{S}_5$ amorphous materials prepared by melt-quenching and mechanical milling. *J. Non-Cryst. Solids* **358**, 93–98, doi:<https://doi.org/10.1016/j.jnoncrysol.2011.08.030> (2012).
23. Dive, A., Zhang, Y., Yao, Y., Martin, S. W. & Banerjee, S. Investigations of the structure of $\text{Na}_2\text{S} + \text{P}_2\text{S}_5$ glassy electrolytes and its impact on Na^+ ionic conductivity through ab initio molecular dynamics. *Solid State Ion.* **338**, 177–184, doi:<https://doi.org/10.1016/j.ssi.2019.05.014> (2019).
24. Bischoff, C., Schuller, K., Dunlap, N. & Martin, S. W. IR, Raman, and NMR Studies of the Short-Range Structures of $0.5\text{Na}_2\text{S} + 0.5[\text{xGeS}_2 + (1-\text{x})\text{PS}_{5/2}]$ Mixed Glass-Former Glasses. *J. Phys. Chem. B* **118**, 1943–1953, doi:10.1021/jp4111053 (2014).
25. Hayashi, A., Noi, K., Sakuda, A. & Tatsumisago, M. Superionic glass-ceramic electrolytes for room-temperature rechargeable sodium batteries. *Nat. Commun.* **3**, 856, doi:10.1038/ncomms1843 (2012).

26. Yu, Z. *et al.* Exceptionally High Ionic Conductivity in $\text{Na}_3\text{P}_{0.62}\text{As}_{0.38}\text{S}_4$ with Improved Moisture Stability for Solid-State Sodium-Ion Batteries. *Adv. Mater.* **29**, 1605561, doi:10.1002/adma.201605561 (2017).
27. Chu, I.-H. *et al.* Room-Temperature All-solid-state Rechargeable Sodium-ion Batteries with a Cl-doped Na_3PS_4 Superionic Conductor. *Sci. Rep.* **6**, 33733, doi:10.1038/srep33733 (2016).
28. Kim, Y., Saienga, J. & Martin, S. W. Anomalous Ionic Conductivity Increase in $\text{Li}_2\text{S} + \text{GeS}_2 + \text{GeO}_2$ Glasses. *J. Phys. Chem. B* **110**, 16318–16325, doi:10.1021/jp060670c (2006).
29. Minami, K., Mizuno, F., Hayashi, A. & Tatsumisago, M. Structure and properties of the $70\text{Li}_2\text{S}\cdot(30 - x)\text{P}_2\text{S}_5\cdot x\text{P}_2\text{O}_5$ oxysulfide glasses and glass-ceramics. *J. Non-Cryst. Solids* **354**, 370–373, doi:<https://doi.org/10.1016/j.jnoncrysol.2007.07.059> (2008).
30. Noi, K., Hayashi, A. & Tatsumisago, M. Structure and properties of the $\text{Na}_2\text{S}-\text{P}_2\text{S}_5$ glasses and glass-ceramics prepared by mechanical milling. *J. Power Sources* **269**, 260–265, doi:<https://doi.org/10.1016/j.jpowsour.2014.06.158> (2014).
31. Hayashi, A., Noi, K., Tanibata, N., Nagao, M. & Tatsumisago, M. High sodium ion conductivity of glass-ceramic electrolytes with cubic Na_3PS_4 . *J. Power Sources* **258**, 420–423, doi:<http://dx.doi.org/10.1016/j.jpowsour.2014.02.054> (2014).
32. Tsukasaki, H., Mori, S., Morimoto, H., Hayashi, A. & Tatsumisago, M. Direct observation of a non-crystalline state of $\text{Li}_2\text{S}-\text{P}_2\text{S}_5$ solid electrolytes. *Sci. Rep.* **7**, 4142, doi:10.1038/s41598-017-04030-y (2017).
33. Jha, P. K., Pandey, O. P. & Singh, K. Structural and thermal properties of $\text{Na}_2\text{S}-\text{P}_2\text{S}_5$ glass and glass ceramics. *J. Non-Cryst. Solids* **379**, 89–94, doi:<https://doi.org/10.1016/j.jnoncrysol.2013.07.009> (2013).
34. Hirai, K., Tatsumisago, M., Takahashi, M. & Minami, T. ^{29}Si and ^{31}P MAS-NMR Spectra of $\text{Li}_2\text{S}-\text{SiS}_2-\text{Li}_3\text{PO}_4$ Rapidly Quenched Glasses. *J. Am. Ceram. Soc.* **79**, 349–352, doi:<https://doi.org/10.1111/j.1151-2916.1996.tb08127.x> (1996).
35. Kmiec, S., Joyce, A. & Martin, S. W. Glass formation and structural analysis of $\text{Na}_4\text{P}_2\text{S}_{7-x}\text{O}_x$, $0 \leq x \leq 7$ sodium oxy-thiophosphate glasses. *J. Non-Cryst. Solids* **498**, 177–189, doi:<https://doi.org/10.1016/j.jnoncrysol.2018.06.007> (2018).
36. Tan, G., Wu, F., Li, L., Liu, Y. & Chen, R. Magnetron Sputtering Preparation of Nitrogen-Incorporated Lithium-Aluminum-Titanium Phosphate Based Thin Film Electrolytes for All-Solid-State Lithium Ion Batteries. *J. Phys. Chem. C* **116**, 3817–3826, doi:10.1021/jp207120s (2012).
37. Jha, P. K., Pandey, O. P. & Singh, K. FTIR spectral analysis and mechanical properties of sodium phosphate glass-ceramics. *J. Mol. Struct.* **1083**, 278–285, doi:<https://doi.org/10.1016/j.molstruc.2014.11.027> (2015).
38. Hayashi, A., Tatsumisago, M., Minami, T. & Miura, Y. Structural Investigation of $95(0.6\text{Li}_2\text{S}_{0.4}\text{SiS}_2)5\text{Li}_4\text{SiO}_4$ Oxysulfide Glass by Using X-ray Photoelectron Spectroscopy. *J. Am. Ceram. Soc.* **81**, 1305–1309, doi:10.1111/j.1151-2916.1998.tb02482.x (1998).

39. Nesbitt, H. W. *et al.* Bridging, non-bridging and free (O^{2-}) oxygen in Na_2O - SiO_2 glasses: An X-ray Photoelectron Spectroscopic (XPS) and Nuclear Magnetic Resonance (NMR) study. *J. Non-Cryst. Solids* **357**, 170–180, doi:<https://doi.org/10.1016/j.jnoncrysol.2010.09.031> (2011).
40. Kim, Y., Saienga, J. & Martin, S. W. Glass formation in and structural investigation of Li_2S + GeO_2 composition using Raman and IR spectroscopy. *J. Non-Cryst. Solids* **351**, 3716–3724, doi:<https://doi.org/10.1016/j.jnoncrysol.2005.09.028> (2005).
41. Hayashi, A., Tanihata, N. & Tatsumisago, M. Development of all solid sodium-sulfur based battery with high capacity using electrolytes containing sulfur compounds. *Electrochemistry (Tokyo, Jpn.)* **82**, 175–180, doi:[10.5796/electrochemistry.82.175](https://doi.org/10.5796/electrochemistry.82.175) (2014).
42. Liu, H. *et al.* Controlling Dendrite Growth in Solid-State Electrolytes. *ACS Energy Lett.* **5**, 833–843, doi:[10.1021/acsenergylett.9b02660](https://doi.org/10.1021/acsenergylett.9b02660) (2020).
43. Ren, Y., Shen, Y., Lin, Y. & Nan, C.-W. Direct observation of lithium dendrites inside garnet-type lithium-ion solid electrolyte. *Electrochim. Commun.* **57**, 27–30, doi:<https://doi.org/10.1016/j.elecom.2015.05.001> (2015).
44. Cheng, E. J., Sharafi, A. & Sakamoto, J. Intergranular Li metal propagation through polycrystalline $Li_{6.25}Al_{0.25}La_3Zr_2O_{12}$ ceramic electrolyte. *Electrochim. Acta* **223**, 85–91, doi:<https://doi.org/10.1016/j.electacta.2016.12.018> (2017).
45. Xu, R., Sun, H., de Vasconcelos, L. S. & Zhao, K. Mechanical and Structural Degradation of $LiNi_xMn_yCo_zO_2$ Cathode in Li-Ion Batteries: An Experimental Study. *J. Electrochem. Soc.* **164**, A3333–A3341, doi:[10.1149/2.1751713jes](https://doi.org/10.1149/2.1751713jes) (2017).
46. Field, J. S., Swain, M. V. & Dukino, R. D. Determination of fracture toughness from the extra penetration produced by indentation-induced pop-in. *J. Mater. Res.* **18**, 1412–1419, doi:[10.1557/jmr.2003.0194](https://doi.org/10.1557/jmr.2003.0194) (2003).
47. McGrogan, F. P. *et al.* Compliant Yet Brittle Mechanical Behavior of Li_2S - P_2S_5 Lithium-Ion-Conducting Solid Electrolyte. *Adv. Energy Mater.* **7**, 1602011, doi:[10.1002/aenm.201602011](https://doi.org/10.1002/aenm.201602011) (2017).
48. Kato, A., Yamamoto, M., Sakuda, A., Hayashi, A. & Tatsumisago, M. Mechanical Properties of Li_2S - P_2S_5 Glasses with Lithium Halides and Application in All-Solid-State Batteries. *ACS Appl. Energy Mater.* **1**, 1002–1007, doi:[10.1021/acsaelm.7b00140](https://doi.org/10.1021/acsaelm.7b00140) (2018).
49. Sakuda, A., Hayashi, A., Takigawa, Y., Higashi, K. & Tatsumisago, M. Evaluation of elastic modulus of Li_2S - P_2S_5 glassy solid electrolyte by ultrasonic sound velocity measurement and compression test. *J. Ceram. Soc. Jpn.* **121**, 946–949, doi:[10.2109/jcersj2.121.946](https://doi.org/10.2109/jcersj2.121.946) (2013).
50. Monroe, C. & Newman, J. The Impact of Elastic Deformation on Deposition Kinetics at Lithium/Polymer Interfaces. *J. Electrochem. Soc.* **152**, A396-A404, doi:[10.1149/1.1850854](https://doi.org/10.1149/1.1850854) (2005).
51. Bonanos, N., Steele, B. C. H. & Butler, E. P. in *Impedance Spectroscopy* 205–537 (John Wiley & Sons: Hoboken, 2005).
52. Irvine, J. T. S., Sinclair, D. C. & West, A. R. Electroceramics: Characterization by Impedance Spectroscopy. *Adv. Mater.* **2**, 132–138, doi:[10.1002/adma.19900020304](https://doi.org/10.1002/adma.19900020304) (1990).

53. Gao, H., Xin, S., Xue, L. & Goodenough, J. B. Stabilizing a High-Energy-Density Rechargeable Sodium Battery with a Solid Electrolyte. *Chem* **4**, 833–844, doi:<https://doi.org/10.1016/j.chempr.2018.01.007> (2018).
54. Seh, Z. W., Sun, J., Sun, Y. & Cui, Y. A Highly Reversible Room-Temperature Sodium Metal Anode. *ACS Cent. Sci.* **1**, 449–455, doi:10.1021/acscentsci.5b00328 (2015).
55. Han, F. *et al.* High electronic conductivity as the origin of lithium dendrite formation within solid electrolytes. *Nat. Energy* **4**, 187–196, doi:10.1038/s41560-018-0312-z (2019).
56. Tian, H.-K., Liu, Z., Ji, Y., Chen, L.-Q. & Qi, Y. Interfacial Electronic Properties Dictate Li Dendrite Growth in Solid Electrolytes. *Chem. Mater.* **31**, 7351–7359, doi:10.1021/acs.chemmater.9b01967 (2019).
57. Lu, X., Xia, G., Lemmon, J. P. & Yang, Z. Advanced materials for sodium-beta alumina batteries: Status, challenges and perspectives. *J. Power Sources* **195**, 2431–2442, doi:<https://doi.org/10.1016/j.jpowsour.2009.11.120> (2010).
58. Song, S., Duong, H. M., Korsunsky, A. M., Hu, N. & Lu, L. A Na⁺ Superionic Conductor for Room-Temperature Sodium Batteries. *Sci. Rep.* **6**, 32330, doi:10.1038/srep32330 (2016).
59. Park, C.-W. *et al.* Discharge properties of all-solid sodium-sulfur battery using poly(ethylene oxide) electrolyte. *J. Power Sources* **165**, 450–454, doi:<https://doi.org/10.1016/j.jpowsour.2006.11.083> (2007).
60. Zhu, T. *et al.* An All-Solid-State Sodium-Sulfur Battery Using a Sulfur/Carbonized Polyacrylonitrile Composite Cathode. *ACS Appl. Energy Mater.* **2**, 5263–5271, doi:10.1021/acsaem.9b00953 (2019).
61. Nagata, H. & Chikusa, Y. An All-solid-state Sodium-Sulfur Battery Operating at Room Temperature Using a High-sulfur-content Positive Composite Electrode. *Chem. Lett.* **43**, 1333–1334, doi:10.1246/cl.140353 (2014).
62. Tanibata, N., Deguchi, M., Hayashi, A. & Tatsumisago, M. All-Solid-State Na/S Batteries with a Na₃PS₄ Electrolyte Operating at Room Temperature. *Chem. Mater.* **29**, 5232–5238, doi:10.1021/acs.chemmater.7b01116 (2017).
63. Yue, J. *et al.* High-Performance All-Inorganic Solid-State Sodium–Sulfur Battery. *ACS Nano* **11**, 4885–4891, doi:10.1021/acsnano.7b01445 (2017).
64. Fan, X. *et al.* High-Performance All-Solid-State Na–S Battery Enabled by Casting–Annealing Technology. *ACS Nano* **12**, 3360–3368, doi:10.1021/acsnano.7b08856 (2018).
65. Ando, T., Sakuda, A., Tatsumisago, M. & Hayashi, A. All-solid-state sodium-sulfur battery showing full capacity with activated carbon MSP20-sulfur-Na₃SbS₄ composite. *Electrochim. Commun.* **116**, 106741, doi:<https://doi.org/10.1016/j.elecom.2020.106741> (2020).

Figures

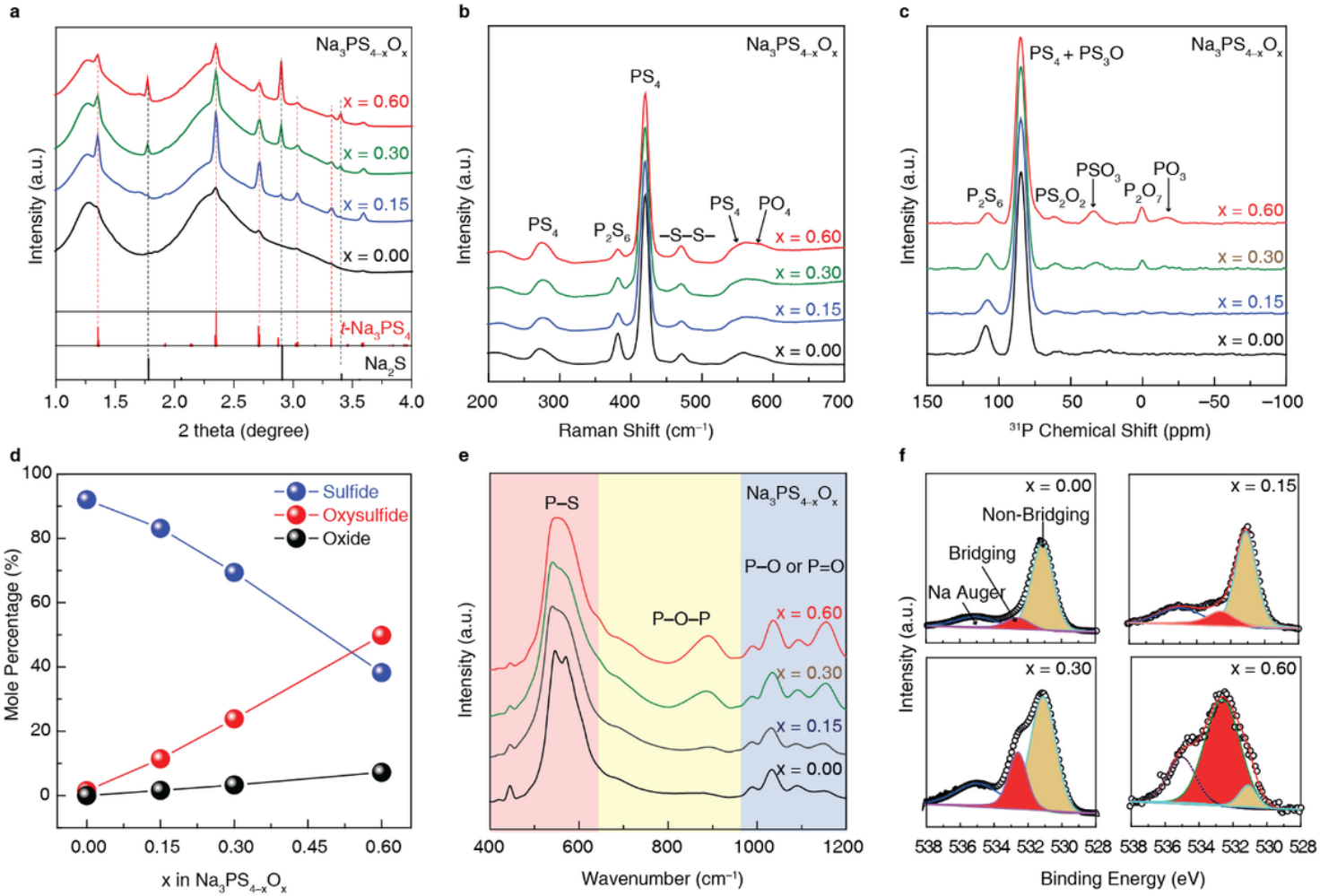


Figure 1

Structural characterizations of $\text{Na}_3\text{PS}_4\text{-xO}_x$ ($x=0, 0.15, 0.30$, and 0.6) SEs. Spectra from (a) synchrotron X-ray diffraction, (b) Raman, (c) ^{31}P NMR, (d) structural units and their relative mol. percentage, (e) Fourier transform-infrared spectra (FTIR), and (f) O 1s X-ray photoelectron (XPS).

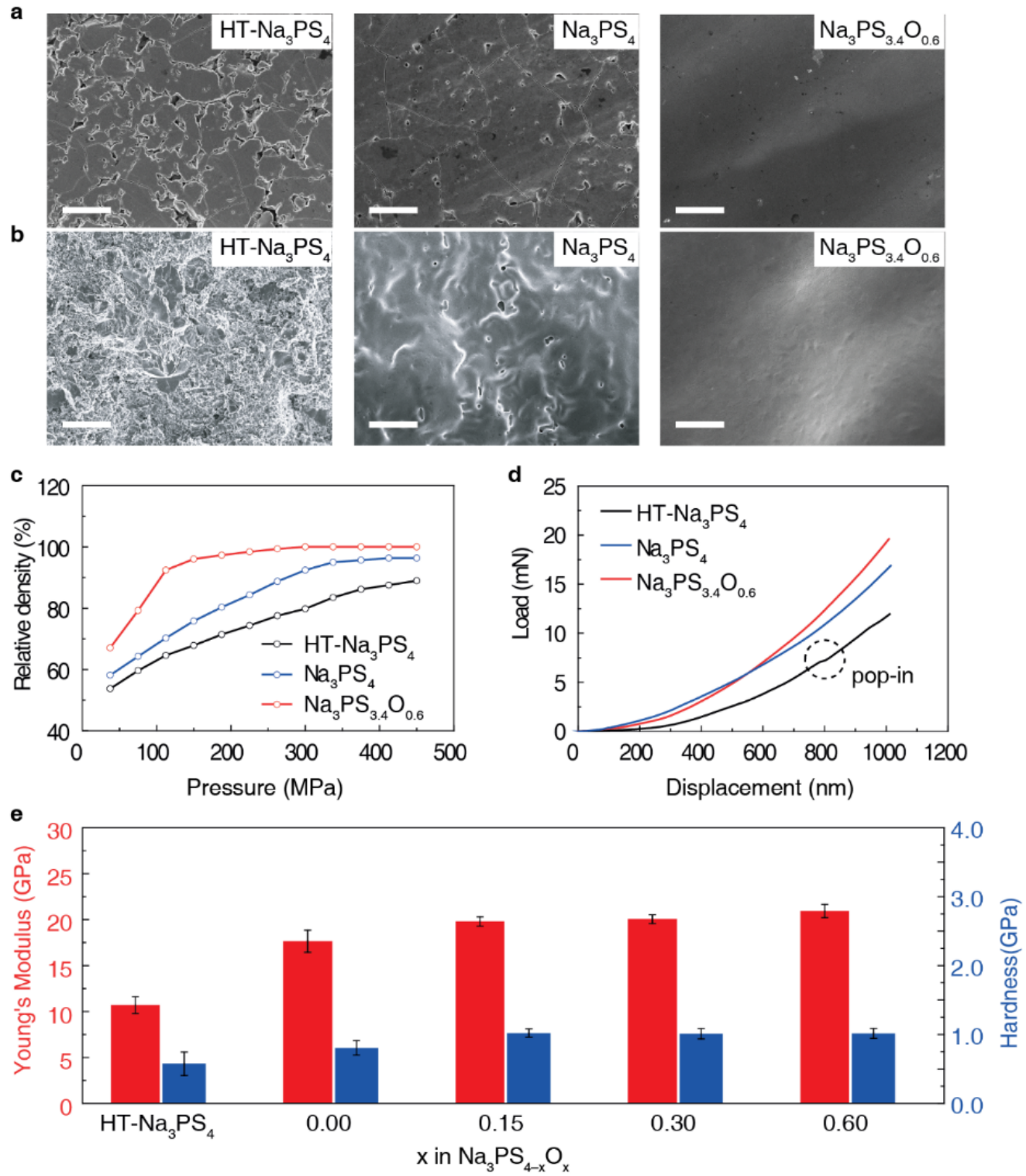


Figure 2

Mechanical properties of $\text{Na}_3\text{PS}_4-\text{xO}_x$ ($\text{x}=0$ and 0.6) glass SEs and HT- Na_3PS_4 glass-ceramic SE. (a) SEM images of the surface and (b) cross-section morphology, scale bar $10 \mu\text{m}$; (c) Relative density vs. fabrication pressure, (d) Nano-indentation loading curves; and (e) Young's modulus and hardness of various SEs.

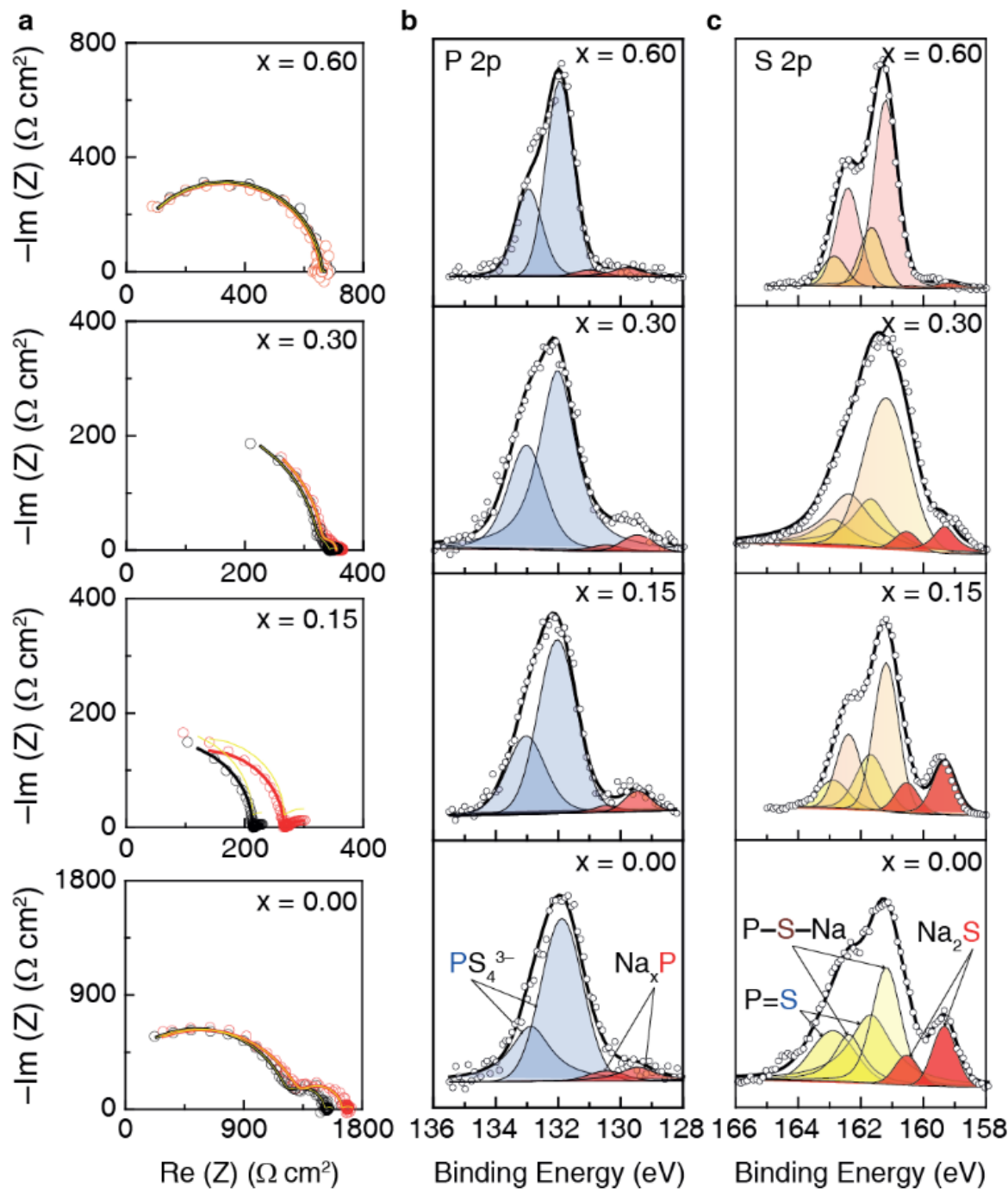


Figure 3

Chemical stability of Na₃PS₄-xO_x (x=0, 0.15, 0.30, and 0.6) SEs towards Na metal at 60 °C. (a) Electrochemical impedance spectra (EIS) evolution of freshly made Na|SE|Na symmetric cells (black curve) vs after 5 hours of rest (red); (b) P 2p and (c) S 2p for the interface between Na and SE, exposed after 5 hours of contact.

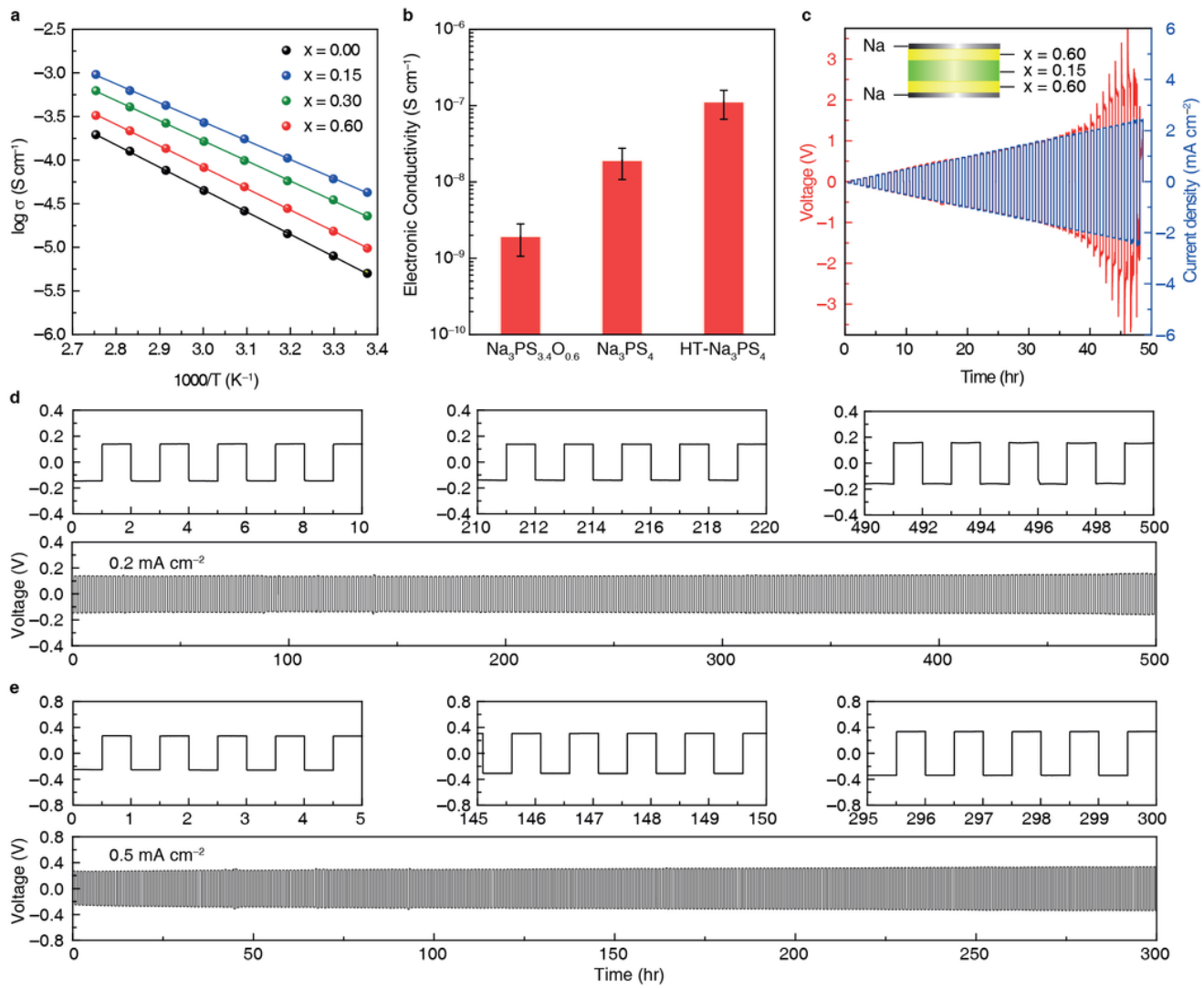


Figure 4

Electrical and electrochemical properties of oxysulfide glassy SEs. (a) Temperature dependence of the Na^+ ion conductivities of SEs; (b) Electronic conductivity of three types of SEs measured by two-blocking electrodes at 60 °C; (c) Critical current density (CCD) test of a tri-layer SE in $\text{Na}|\text{SE}|\text{Na}$ symmetric cell ($\text{Na}_3\text{PS}_3.400.6|\text{Na}_3\text{PS}_3.8500.15|\text{Na}_3\text{PS}_3.400.6$) at 60 °C. The step current density increase is 0.05 mA cm $^{-2}$ and plating/stripping time is 0.5 hour each; (d) and (e) galvanostatic cycling of the symmetric cells at 60 °C under current densities of 0.2 mA cm $^{-2}$ and 0.5 mA cm $^{-2}$, respectively.

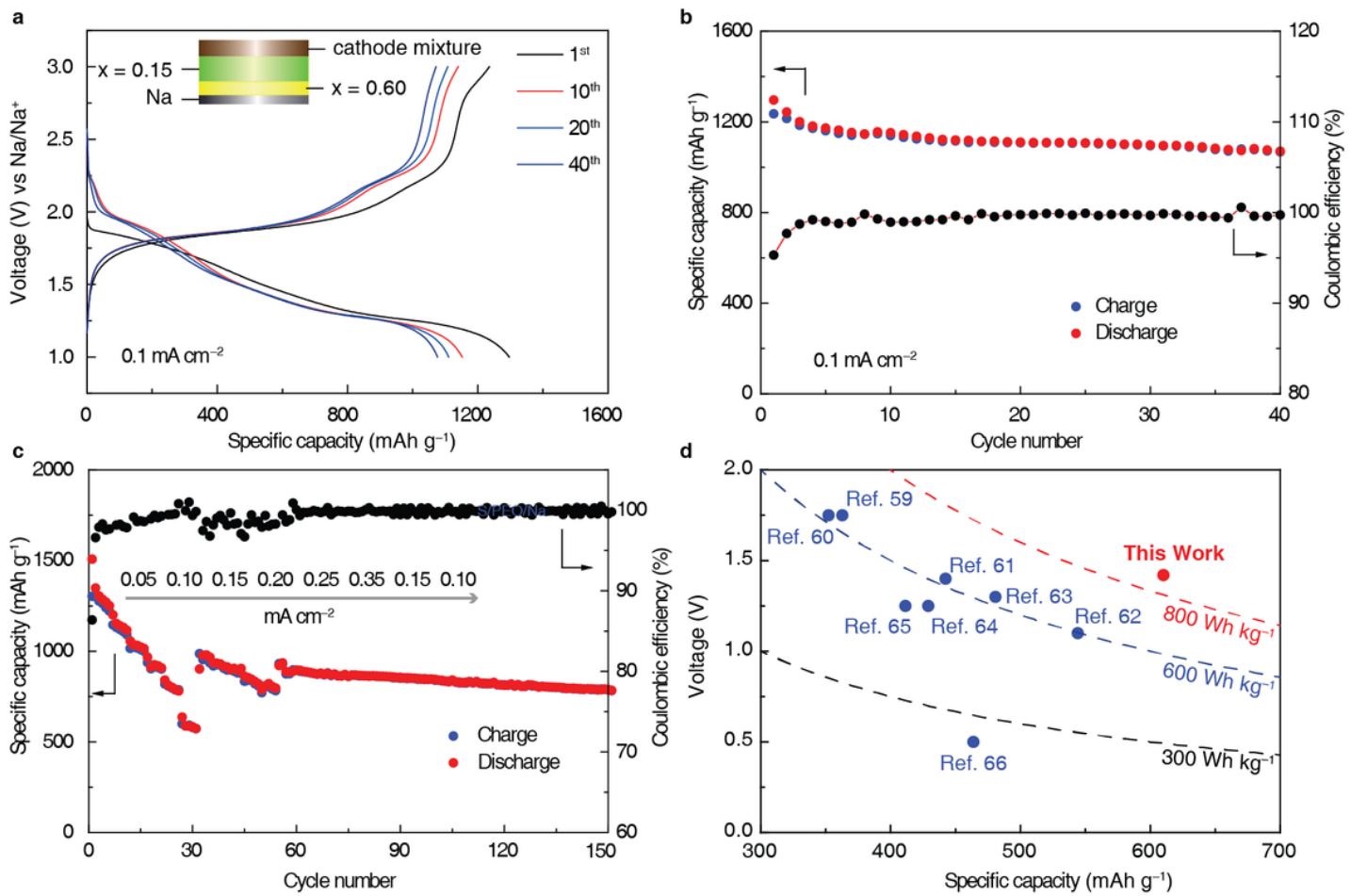


Figure 5

All-solid-state Na–S full cells measured at 60°C . (a) Charge-discharge voltage profiles and (b) Capacity and coulombic efficiency vs. cycle number at a current density of 0.1 mA cm^{-2} ; (c) Rate capabilities of the Na–S full cell under different current densities (0.05 – 0.35 mA cm^{-2}); (d) Summary of cell voltage–full cell capacity plot and material-level specific energy for reported ambient-temperature solid-state Na–S batteries. See supplementary Table S3 for details.

Supplementary Files

This is a list of supplementary files associated with this preprint. Click to download.

- [SupplementaryInformation.docx](#)